https://doi.org/10.5194/egusphere-2026-3360
Preprint. Discussion started: 13 July 2026

Cross-phase partitioning of sulfur-nitrogen ratios and aerosol mixing-state evolution based on single-particle observations

Yuan Dai[1,2], Junfeng Wang[1*], Mindong Chen[1], Su Zhang[2], Haiwei Li[1], Yunjiang Zhang[1], Yun Wu[1], Ming Wang[1], Xinlei Ge[3*]

[1]*Jiangsu Key Laboratory of Atmospheric Environment Monitoring and Pollution Control (AEMPC), Collaborative Innovation Center of Atmospheric Environment and Equipment Technology (CIC-AEET), School of Environmental Science and Engineering, Nanjing University of Information Science and Technology, Nanjing 210044, China*
[2]*Yangzhou Environmental Monitoring Center, Yangzhou 225009, China*
[3]*School of Energy and Environment, Southeast University, Nanjing 211189, China*

Correspondence: Xinlei Ge (xinlei@seu.edu.cn), Junfeng Wang (wangjunfeng@nuist.edu.cn)

https://doi.org/10.5194/egusphere-2026-3360
Preprint. Discussion started: 13 July 2026

Abstract

Understanding sulfur-nitrogen partitioning is essential for predicting secondary aerosol formation and mixing-state evolution, yet the mechanisms governing its cross-phase coupling remain poorly constrained. Here, we integrate single-particle mass spectrometry (SPA-MS) with air-pollutant and meteorological observations from two regional emission-control periods. We define three sulfur-to-nitrogen ratio metrics in the gas (gSNR), particle (pSNR), and number-based (nSNR) domains, and use causal inference and interpretable machine learning to identify their linkages and environmental drivers. The results reveal a stepwise propagation from precursor composition to particle chemistry and then to population mixing-state evolution. Although gSNR sets the first-order constraint on sulfur-nitrogen partitioning, the aerosol response is strongly particle-type dependent, with more pronounced sulfate enrichment in black-carbon-containing and organic-rich particles than in BC-free particles. Relative humidity (RH) emerges as the primary regulator of this coupling by modulating aerosol liquid water and phase transitions. Under dry conditions, the three SNR metrics diverge and aerosols remain largely externally mixed; under humid conditions, the metrics converge and aerosols evolve toward a more internally mixed state. Our results support the inclusion of RH- and particle-type-dependent parameterizations of cross-phase coupling and chemical heterogeneity in air-quality models.

https://doi.org/10.5194/egusphere-2026-3360
Preprint. Discussion started: 13 July 2026

1. Introduction

Secondary aerosols, dominated by sulfate and nitrate, constitute a major fraction of fine particulate matter ($PM_{2.5}$, aerodynamic diameter ⩽ 2.5 μm)(Huang et al., 2014; Wang et al., 2013). These species strongly influence aerosol hygroscopicity, toxicity, optical properties, and radiative forcing (Nozière et al., 2010; Sheldon et al., 2023; El Haddad et al., 2024). They originate mainly from the multiphase oxidation of sulfur dioxide (SO_2) and nitrogen oxides ($NO_x = NO_2 + NO$) (Cheng et al., 2016; Liu et al., 2022) and their formation is governed by the interplay of precursor abundance, atmospheric oxidizing capacity, and meteorological conditions (George and Abbatt, 2010; Shiraiwa et al., 2011; Wen et al., 2018). Among these factors, relative humidity (RH) plays a central role by regulating aerosol liquid water and phase state, which in turn influences surface properties, mass-transport rates, and chemical aging pathways (Shiraiwa et al., 2011; Liu et al., 2018; Huang et al., 2023). These coupled processes are concisely reflected in the sulfur-to-nitrogen ratio (SNR), a common diagnostic for source attribution and sulfate-nitrate (S-N) evolution (Xie et al., 2020; Liu et al., 2020; Sosa Echeverría et al., 2023). However, SNR is still often interpreted using bulk or time-averaged measurements (Snider et al., 2016; Sun et al., 2016; Xu et al., 2019), which may inherently obscure particle-type heterogeneity and mixing-status diversity that matter for multiphase processing. Furthermore, current model parameterizations often oversimplify the effects of RH and aerosol phase state (Schmedding et al., 2020; Shiraiwa et al., 2017), while observational constraints remain largely limited to heavily polluted episodes (Huang et al., 2023; J. Wang et al., 2021). These limitations leave uncertainties regarding how shifts in gas-phase precursor composition translate into particle composition, number fractions, and transitions between internal and external mixing, particularly under cleaner urban conditions.

These uncertainties may be magnified by the rapid evolution of anthropogenic emissions. Between 2013 and 2024, China's clean air actions triggered an asymmetric decline in major gaseous precursors (Y. Zhang et al., 2020; Geng et al., 2024): annual SO_2 fell from 40 to 8 μg m^{-3} (−80%) and stabilized well below the World Health Organization (WHO) guidelines, while NO_2 reductions were more moderate (−55%), remaining nearly twice the revised WHO annual limit (Ministry of Ecology and Environment of the People's Republic of China. Bulletins on the State of China's Ecological and Environmental Quality, 2013–2024. https://www.mee.gov.cn/hjzl/sthjzk/zghjzkgb/). This imbalance drove the national gas-phase SNR (gSNR) down from 1.27 to 0.56 and favored nitrate-dominated aerosols (Liu et al., 2022; Chu et al., 2020; Lin et al., 2023). However, further trend shifts are likely as policy priorities move toward deeper NO_x control. The WHO tightened its annual NO_2 guideline (from 40 to 10 μg m^{-3}), while relaxing the daily SO_2 limit (from 20 to 40 μg m^{-3}). China has strengthened industrial and traffic NO_x emission standards (Lu et al., 2020; Y. Zhang et al., 2021), and accelerated the uptake of new-energy

https://doi.org/10.5194/egusphere-2026-3360
Preprint. Discussion started: 13 July 2026

vehicles (Liang et al., 2019). Under this trend, gSNR may rise again, potentially coinciding with higher ozone (O_3) levels and a more oxidizing atmosphere(Li et al., 2019). The COVID-19 lockdowns provide a natural experiment consistent with this direction. Across Chinese megacities, lockdown periods induced sharp, short-term NO_x declines (30% to 50%) and O_3 increases (21% to 77%) while SO_2 remained stable (Le et al., 2020; Huang et al., 2021; Dai et al., 2024), effectively simulating future emission trends within a cleaner and more oxidizing background.

In this study, we use these perturbations in Yangzhou, a representative city in the Yangtze River Delta (YRD), to investigate multiphase S-N evolution across two lockdown-recovery cycles. By integrating single-particle aerosol mass spectrometry (SPA-MS) with causal inference and interpretable machine-learning analysis, we track S-N partitioning across gas, particle and number domains. This particle-resolved approach links precursor shifts, oxidizing conditions, and RH-dependent phase transitions to single-particle aging and mixing-state evolution, providing process-level evidence to improve regional model representations of coupled S-N partitioning under ongoing NO_x mitigation.

2. Methods

2.1 Site Description and Sampling Periods

Field observations were conducted at a national air-quality monitoring station in Yangzhou (32.41°N, 119.40°E), a representative urban center within the YRD of China. The monitoring site is situated 20 m above ground level in a mixed residential, commercial, and educational district, representing typical urban background conditions in the region. To examine atmospheric responses to abrupt emission changes during the COVID-19 pandemic, we selected four rain-free five-day episodes with broadly comparable meteorological conditions, comprising two emission control periods (ECPs) and their corresponding normal periods (NPs): a winter ECP (W-ECP, 29 January–2 February 2020) and its winter NP (W-NP, 20–24 February 2020), as well as a summer ECP (S-ECP, 17–21 August 2021) and its summer NP (S-NP, 17–21 September 2021).

Single-particle chemical composition, size, and mixing state were measured in real time using a single-particle aerosol mass spectrometer (SPA-MS; Hexin Analytical Instrument Co., Ltd., China), as detailed previously (Dai et al., 2024). Concurrently, $PM_{2.5}$ mass concentrations were measured by a particulate matter monitor (XHPM2000E, Xianhe, China), while trace gases (NO_x, SO_2, CO, and O_3) were quantified using Thermo Scientific analyzers (Models 42i, 43i, 48i, and 49i) (**Figure S1**). All instruments were co-located to ensure the temporal and spatial consistency of the aerosol and precursor datasets.

https://doi.org/10.5194/egusphere-2026-3360
Preprint. Discussion started: 13 July 2026

Meteorological parameters were retrieved via Google Earth Engine (GEE) from the NASA Goddard Earth Observing System Composition Forecast system (GEOS-CF) and the ERA5-Land hourly dataset from the European Centre for Medium-Range Weather Forecasts (ECMWF). Ten variables were extracted for the grid cell nearest to the monitoring site (**Table S2**): 2 m air temperature (T2m), 10 m air temperature (T10m), eastward and northward wind components at 2 m (U2m, V2m), surface net solar radiation (SSR), planetary boundary layer height (BLH), sea level pressure (SLP), total precipitation (TPREC), 2 m dew point temperature (DP2m), and relative humidity (RH). These variables were selected for their potential roles in influencing atmospheric stability, pollutant transport, and chemical transformation kinetics. All datasets were temporally synchronized to an hourly resolution to facilitate integrated analysis with the chemical measurements.

2.2 Single-Particle Classification

A total of 324,090 ambient particles were detected and classified based on their SPA-MS mass spectra. Particles were clustered using the ART-2a algorithm in MATLAB R2024a (MathWorks, Inc.) via the Computational Continuation Core toolkit (COCO v1.4). The algorithm was executed for 20 iterations with a vigilance factor of 0.8 and a learning rate of 0.05, parameters consistent with established single-particle aerosol studies (Huang et al., 2023; G. Zhang et al., 2021; Dai et al., 2024). Following the initial clustering, particle types were aggregated into five operational principal groups according to their dominant mass-spectral signatures. Black Carbon (BC) particles were identified by carbon-cluster ions (e.g., m/z $\pm12[C]^{+/-}$, $\pm36[C_3]^{+/-}$, $\pm48[C_4]^{+/-}$, and $\pm60[C_5]^{+/-}$). BC with organic carbon (BCOC) particles exhibited the same BC signatures together with characteristic organic-carbon (OC) fragments (e.g., m/z $27[C_2H_3]^+$, $29[C_2H_5]^+$, $37[C_3H]^+$, and $43[C_2H_3O]^+$). BC-free inorganic (BF) particles lacked BC cluster signatures and were dominated by inorganic species. BC-free OC-rich (BFOC) particles also lacked BC clusters but showed a high relative abundance of OC fragments. Residual subclasses with mixed or ambiguous signatures were defined as “Other”.

To better resolve S-N partitioning, we further divided these principal groups into 19 subclasses. Subclasses enriched in secondary inorganic species (SIS) were identified by sulfate ($-97[HSO_4^-]$, $-96[SO_4^{2-}]$), nitrate ($-62[NO_3^-]$, $-46[NO_2^-]$), or both, and were labeled with the suffixes “-S”, “-N” and “-SN”, respectively. Particles exhibiting strong cyanide-related ions ($-26[CN^-]$ and $-42[CNO^-]$) were labeled with “-CN”. Number fractions and representative mass spectra are summarized in Supplementary **Table S1** and **Figure S2**.

https://doi.org/10.5194/egusphere-2026-3360
Preprint. Discussion started: 13 July 2026

2.3 Fresh-like and Aged-like Particles Categorization

Aerosols were further grouped into fresh-like (-CN) and aged-like (-sec) based on diagnostic SPA-MS fragments and vacuum aerodynamic diameter (D_{va}) (**Figure 1f** and **Figure 2**). Strong cyanide-related ions together with carbonaceous fragments are commonly observed in relatively fresh combustion particles from biomass burning, coal combustion, and vehicle exhaust (Huang et al., 2023; Sun et al., 2017; G. Zhang et al., 2020). We therefore treated CN-containing subclasses within each principal group as operational fresh-like states. For instance, BCOC-CN particles exhibit abundant carbon-cluster and hydrocarbon fragments accompanied by cyanide signatures (**Figure 2h**), occurring predominantly at smaller D_{va} (100−600 nm), consistent with freshly emitted combustion aerosols (Sharma et al., 2018). Similarly, BFOC-CN particles display +39[K^+], −26[CN^-], and levoglucosan-derived fragments (−45[CHO_2^-], −59[$C_2H_3O_2^-$], −73[$C_3H_5O_2^-$]) also appear at small sizes, representing primary organic aerosol from biomass burning (**Figure 2c**) (Bi et al., 2011; Huang et al., 2023).

Aged-like types (-sec) were constructed by regrouping sulfate-rich (-S), nitrate-rich (-N) and mixed (-SN) subclasses into composite SIS-enriched categories within each principal group, reflecting extensive secondary processing (Xie et al., 2020). BCOC-sec types display coexisting BC, OC and strong SIS fragments (**Figure 2g**), indicating substantial internal mixing of carbonaceous and secondary inorganics, in line with previous observations (Dai et al., 2024; Xie et al., 2020). BC-sec (BC-S, -N, -SN; **Figure 2f** showed negligible OC signals but elevated SIS ions, while BF-sec and BFOC-sec (BF-S, -N, -SN; BFOC-S, -N, -SN) exhibit elevated sulfate and nitrate ions but lack BC fragments (**Figure 2b, d**).

The consistency of this fresh-aged framework is supported by both compositional and temporal behavior. The fraction of SIS signal is systematically lower in "-CN" than in "-sec" types for BC, BCOC, BF and BFOC groups (**Figure S3a**). In addition, hourly number concentrations of each "-sec" type correlate most strongly with the "-CN" type within the same principal group (**Figure S3b**). Together with the systematic increase in D_{va} from "-CN" to "-sec", these diagnostics support interpreting "-CN" and "-sec" as early- and late-stage states within each principal group. We therefore define four dominant fresh/aged pairs: BC-CN/BC-sec, BCOC-CN/BCOC-sec, BF-CN/BF-sec, and BFOC-CN/BFOC-sec.

2.4 Definition of Sulfur-to-Nitrogen Ratios (SNR) Metrics

To quantify S-N partitioning across gas, particles, and number domains, we define three complementary SNR metrics: gas-phase SNR (gSNR), particle-phase SNR (pSNR), and number-based SNR (nSNR). The gSNR is calculated as the molar ratio of SO_2 to

https://doi.org/10.5194/egusphere-2026-3360
Preprint. Discussion started: 13 July 2026

NO_x from hourly observations:

$$\mathrm{gSNR} = \frac{[SO_2]}{[NO_x]}.$$

The pSNR is derived from SPA-MS spectra by calculating the ratio of total peak areas (PA) of sulfate ions ($-97[HSO_4^-]$, $-96[SO_4^{2-}]$) to nitrate ions ($-62[NO_3^-]$, $-46[NO_2^-]$) for selected single-particle or particle class:

$$\mathrm{pSNR} = \frac{\mathrm{PA_{sulfate}}}{\mathrm{PA_{nitrate}}}.$$

Although SPA-MS is semi-quantitative, this within-spectrum ratio provides a robust relative proxy because both ion species are detected under identical acquisition conditions. Consequently, pSNR is interpreted as a relative indicator rather than an absolute mass ratio, consistent with prior SPA-MS studies (Healy et al., 2013; G. Zhang et al., 2021).

The nSNR represents the ratio of the number concentrations (N) of sulfur-containing particles to nitrogen-containing particles, serving as a population-level proxy for external mixing tendency of sulfate- versus nitrate-containing particles:

$$\mathrm{nSNR} = \frac{N_{\mathrm{sulfur-containing}}}{N_{\mathrm{nitrogen-containing}}}.$$

2.5 Particle-Type-Resolved Hygroscopicity Estimation

To quantify hygroscopic behavior in a particle-type-resolved manner, we estimated an effective hygroscopicity parameter (κ_{eff}) for each particle class at hourly resolution based on aggregated SPA-MS ion signals. For a given particle class, major ion peaks were assigned to several chemical components (e.g., sulfate, nitrate, organics, black carbon, and potassium salts). For each component i, the hourly summed peak area A_i was normalized by its assumed density ρ_i (e.g., ammonium nitrate for nitrate, ammonium sulfate for sulfate; **Table S3**) to obtain an equivalent volume. The volume fraction of component i was then approximated as

$$\varepsilon_i \approx \frac{A_i/\rho_i}{\sum_j (A_j/\rho_j)}.$$

The effective hygroscopicity of each particle class was calculated using κ-Köhler theory and the Zdanovskii-Stokes-Robinson (ZSR) mixing rule (Petters and Kreidenweis, 2007):

$$\kappa_{\mathrm{eff}} = \sum_i (\varepsilon_i \times \kappa_i),$$

where κ_i is the literature-derived hygroscopicity parameter of component i (**Table S3**). Thus, κ_{eff} represents the hourly average hygroscopicity of each particle type inferred from single-particle mass spectra. Given that SPA-MS signals are semi-quantitative and

https://doi.org/10.5194/egusphere-2026-3360
Preprint. Discussion started: 13 July 2026

component-dependent, and that nitrate and sulfate are represented as ammonium salts under an internal-mixing, ideal-ZSR assumption, κ_{eff} is interpreted as a relative, particle-type-resolved hygroscopicity indicator. We use κ_{eff} to compare hygroscopicity among particle classes and episodes and to examine hygroscopic aging pathways, rather than to derive absolute cloud-condensation nuclei (CCN) activation properties.

2.6 Causal Inference Analysis

Causal networks, expressed as directed acyclic graphs (DAGs), capture conditional dependencies and facilitate the inference of potential cause-effect pathways among variables (Koller, 2009). In this study, we applied the Causal Learner toolbox in MATLAB R2024a (MathWorks, Inc.) (Ling et al., 2022) to identify key interactions among SNR metrics, meteorological parameters, and gaseous pollutants.

For each target SNR metric (gSNR, pSNR, nSNR), the Grow-Shrink (GS) algorithm was first applied to determine its Markov blanket (MB), the minimal variable set directly linked to the target. The GS procedure alternates between adding conditionally dependent variables (grow phase) and removing conditionally independent variables (shrink phase) until convergence (Margaritis, 1999). The MB-derived subset was further refined using the Greedy Equivalence Search (GES) algorithm, which iteratively improves the global causal structure via adding edges (forward phase) and removing redundant links to prevent overfitting (backward phase) (Chickering, 2003). The resulting DAGs revealed both direct and indirect pathways connecting SNR evolution to its meteorological and chemical drivers, providing a robust causal foundation for subsequent predictive modeling.

2.7 SSA-XGBoost Modeling and Interpretation

Building on the DAG-derived causal structure, we used the eXtreme Gradient Boosting (XGBoost) algorithm to construct separate models for each aged-like particle class (BCOC-sec, BC-sec, BFOC-sec, BF-sec), with hourly pSNR and nSNR modeled in turn as target variables, to quantify the relative influence of the identified drivers on their variability. All predictors were standardized by the z-score method before model fitting. The dataset was split into six folds: five folds for iterative training and validation, and one held-out fold reserved exclusively for interpretation to prevent information leakage. Model hyperparameters were tuned via the Sparrow Search Algorithm (SSA), a swarm-intelligence metaheuristic that balances global exploration (discoverer phase) and local exploitation (joiner phase) to prevent premature convergence (Yang et al., 2025). SSA was run with a population size of 10 and 50 iterations. Model performance was assessed using root-mean-square error (RMSE) and the coefficient of determination (R^2), averaged over five validation folds (**Table S4**). The SSA-XGBoost model achieved high R^2 (0.71–0.91) for major particle types, ensuring the robustness

https://doi.org/10.5194/egusphere-2026-3360
Preprint. Discussion started: 13 July 2026

of the predicted SNR values.

We interpreted the trained models using SHapley Additive exPlanations (SHAP), a cooperative game-theoretic approach that decomposes individual predictions into additive feature contributions (Ekanayake et al., 2022). SHAP values quantify both the magnitude and direction of each predictor's effect on pSNR or nSNR. This approach provides transparent and physically meaningful insights into how gSNR, meteorology, and gaseous pollutants modulate SNR variability across aged-like particle types.

3. Results and discussion

3.1 Atmospheric Responses to Emission Shifts

Using the four episodes defined in **Section 2.1**, we assessed atmospheric responses to abrupt anthropogenic emission shifts across two COVID-19 ECP and NP cycles in Yangzhou (**Figure 1** and **Figure S1**). During the ECPs, surface NO_x concentrations decreased sharply relative to the corresponding NPs, by 39% in winter and 34% in summer (**Figure 1a**). In contrast, SO_2 changed little and remained within 3.5 to 3.9 ppb. This asymmetric response significantly enhanced gSNR, with seasonal averages increasing from 0.21 to 0.36 (+71%) in winter and from 0.35 to 0.56 (+60%) in summer. O_3 was about 15% higher during ECPs, consistent with weaker NO titration (Wang et al., 2022). $PM_{2.5}$ decreased modestly during ECPs, by 13% in winter and 9% in summer (**Figure 1a**).

Time series show that gSNR, pSNR, and nSNR varied synchronously, and their fluctuations were more distinct during ECPs than during NPs (**Figure 1c**). This co-variation indicates that changes in precursor composition were accompanied by coherent responses in particle composition and in the population-level abundance of sulfur- and nitrogen-containing aerosols. Total particle number concentration (N) increased during NPs while $PM_{2.5}$ mass remained similar, suggesting a shift toward smaller particles that contribute more strongly to number than to mass after controls were relaxed (**Figure 1d**).

As shown in **Figure 1b**, BC-containing particles dominated the aerosol population across all episodes, accounting for an average of 58% of total detections and peaking at 69% during S-ECP. Freshly emitted particles accounted for approximately 16% of detections during ECPs and rose to ~26% in the NPs, reflecting the rebound in primary emissions. Relative to NPs, ECPs were associated with more sulfate-dominated secondary inorganic species (SIS) and pronounced particle growth across particle classes. Averaged across all categories, pSNR was about 57% higher during ECPs than during NPs (**Figure 1e**), with a stronger shift in BC-containing than in BC-free particles and a larger contrast in summer than in winter. Mean D_{va} was increased by about 27%

https://doi.org/10.5194/egusphere-2026-3360
Preprint. Discussion started: 13 July 2026

during ECPs, with the largest increases in aged-like types (**Figure 1f**). Across all principal groups, aged-like categories consistently showed higher pSNR and broader size distributions than their fresh-like counterparts, consistent with enhanced oxidation under elevated gSNR, favoring sulfate-rich growth.

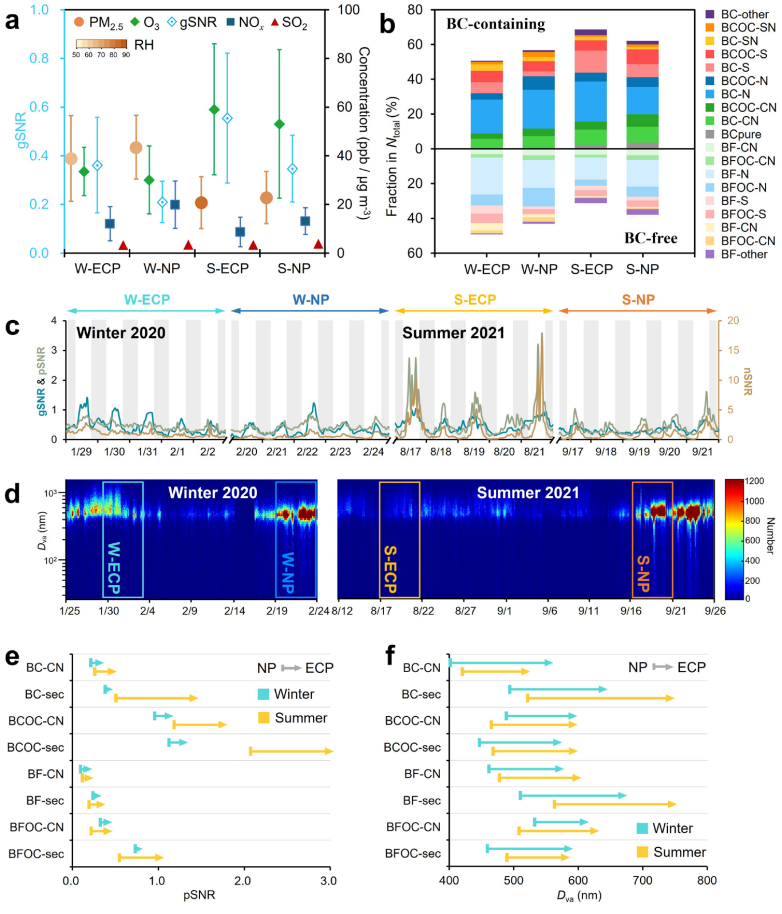

Figure 1. Physicochemical characteristics of particles under different emission control and normal periods. W-ECP, W-NP, S-ECP and S-NP denote the winter emission control period, winter normal period, summer emission control period and summer normal period, respectively. (a) Variations in the gas-phase sulfur-to-nitrogen ratio (gSNR) alongside major atmospheric constituents. (b) Number fractions of BC-containing and BC-free particle types. (c) Temporal profiles of gSNR, particle-phase SNR (pSNR) and number-based SNR (nSNR). (d) Temporal evolution of size-resolved total particle number distributions; D_{va} denotes the vacuum aerodynamic diameter of single particles. (e-f) Seasonal contrasts in pSNR and D_{va} of different particle types between emission control periods (ECPs) and normal periods (NPs).

https://doi.org/10.5194/egusphere-2026-3360
Preprint. Discussion started: 13 July 2026

3.2 Composition-Dependent Diurnal Modulation of Particle-Phase Sulfur-to-Nitrogen Ratio

To quantify compositional effects on pSNR variation, representative aged-like particles were decomposed into BC, OC, and SIS components (**Figure 2**). The BF-sec group was used as the non-carbonaceous reference. To quantify the relative sulfate-to-nitrate enrichment in carbonaceous particles, we defined a normalized pSNR enhancement factor (λ) as follows:

$$\lambda_i = \frac{\mathrm{pSNR}_i}{\mathrm{pSNR}_{\mathrm{BF\text{-}sec}}},$$

where i corresponds to BFOC-sec, BC-sec, and BCOC-sec particle types, yielding λ_{OC}, λ_{BC}, and λ_{BCOC}, respectively.

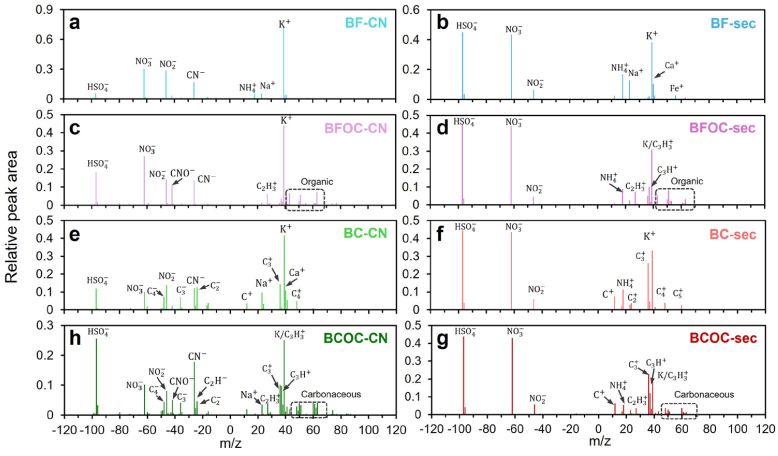

Figure 2. Representative single-particle mass spectra of fresh-like (-CN) and aged-like (-sec) particle classes.

Figure 3 shows pronounced diurnal and seasonal contrasts in λ, with larger amplitudes and greater variability in summer. A distinct daytime transition is evident in summer, with λ_{BC} rising from 1–3 in the morning to 6–9 near local solar noon, exceeding λ_{OC} (typically 3–6) and remaining dominant until evening (**Figure 3d**). This behavior is consistent with the hypothesis of enhanced sulfate formation on BC-containing particles during photochemically active periods, potentially linked to BC-mediated HONO/NO_2 release (Liang et al., 2021; Ye et al., 2017) and photo-induced the formation of reactive oxygen species (ROS) that accelerate the conversion of SO_2-to-sulfate (Zhang et al., 2022; Zhu et al., 2020). At night, when solar radiation is negligible and RH is high (>80%), λ_{OC} exceeds λ_{BC}, aligning with aqueous-phase sulfate production through H_2O_2 or O_3 oxidation and with possible organosulfate formation (Cheng et al., 2016; Y. Wang et al., 2021). Increased organic-phase viscosity may further limit gas-particle partitioning (Vaden et al., 2011), water uptake (Rickards et al., 2015), and multiphase reactions (Shiraiwa et al., 2011), which could prolong sulfate

https://doi.org/10.5194/egusphere-2026-3360
Preprint. Discussion started: 13 July 2026

retention within OC-rich particles. Laboratory and modeling studies also suggest that BC can catalyze SO_2 oxidation even in darkness (He et al., 2018; He and He, 2020), although this likely represents a minor nighttime pathway compared with OC-driven aqueous processes.

Across the summer diurnal cycle, λ_{BCOC} consistently exceeds both λ_{BC} and λ_{OC}, peaking in the afternoon (**Figure 3d**). This persistent enhancement suggests a synergistic role of BCOC, BC provides reactive or catalytic surfaces, while OC facilitates sulfate accommodation or retention within the particle matrix. Such synergy likely reflects the complex surface chemistry of BC, involving polycyclic aromatic hydrocarbons (PAHs) and aromatic oxygenated species, which may promote SO_2 uptake and facilitate heterogeneous oxidation under ultraviolet (UV) irradiation (Riva et al., 2016). Light-absorbing organic compounds, such as brown carbon and humic-like substances, may further act as photosensitizers and accelerate SO_2-to-sulfate conversion (X. Wang et al., 2020).

In winter (**Figure 3a, b**), all λ values are smaller, but the compositional contrasts remain. λ_{OC} generally exceeds λ_{BC} throughout the day, consistent with a larger relative contribution of OC-related aqueous pathways under weaker photochemistry. Nevertheless, λ_{BCOC} remains the largest, indicating that BCOC mixtures still provide the most favorable environment for sulfate enrichment even under low-radiation, low-temperature conditions. This persistent BCOC advantage may reflect not only enhanced photochemical/heterogeneous processing, but also microphysical effects, such as larger accessible surface associated with soot morphology (Beeler et al., 2025) and coating softening or water uptake (Li et al., 2021) that promotes sulfate partitioning and retention.

These observations show that the diurnal variation of pSNR is strongly composition-dependent. BC-containing particles show the strongest enhancement during photochemically active hours, OC-rich particles become relatively more important under humid nighttime and winter conditions, and mixed BCOC particles show the largest enhancement in both seasons, likely driven by combined chemical and microphysical effects.

https://doi.org/10.5194/egusphere-2026-3360
Preprint. Discussion started: 13 July 2026

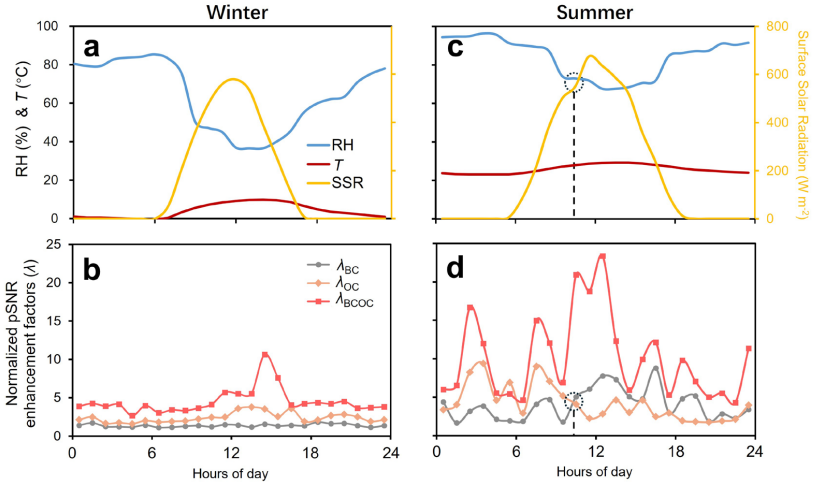

Figure 3. Diurnal cycles of meteorology and component-resolved particle-phase sulfur-to-nitrogen ratio (pSNR) enhancement (λ) in winter (a, b) and summer (c, d). (a, c) show the diurnal variation of meteorological parameters, including relative humidity (RH, blue), temperature (*T*, deep red), and surface solar radiation (SSR, yellow). (b, d) present normalized pSNR enhancement factors (λ) values for components: organic carbon (λ_{OC}; pink), black carbon (λ_{BC}; black), and the mixed BC-OC (λ_{BCOC}; red). The dashed circles indicate the transitional period when BC overtakes OC in driving pSNR enhancement during summer.

3.3 Multistage Hygroscopic-Chemical Aging Pathways Across Particle Classes

To further resolve the aging behavior of distinct particle classes, we analyzed the co-evolution of hygroscopicity and composition within a core-shell framework and mapped aging pathways in the κ_{eff}-pSNR space (**Figure 4**). As defined in **Section 2.3**, each fresh-like subtype is paired with its dominant aged-like counterpart. We identified two sequential regimes: Stage I represents aging under moderate gSNR and oxidation during NPs, when fresh-like particles transition toward aged-like states. Stage II represents additional processing of the Stage I products under elevated gSNR and stronger oxidation during ECPs. Across classes, aging pathways generally trend toward higher hygroscopicity (κ_{eff}), greater pSNR, and larger size (D_{va}), though these changes are more pronounced in summer than in winter (**Figure 4**). On average, Stage II increases κ_{eff} by ~5%, pSNR by ~80%, and D_{va} by ~30%, indicating substantial additional aging. These pathways remain strongly composition-dependent and reflect differences in core type, coating chemistry, and mixing state.

For OC-rich fresh particles (BCOC-CN and BFOC-CN), aging proceeds in two steps.

https://doi.org/10.5194/egusphere-2026-3360
Preprint. Discussion started: 13 July 2026

During Stage I, D_{va} decreases by ~5% while pSNR rises by ~83%, with little change in κ_{eff}. This pattern suggests compaction accompanied by the formation of a dense organic shell that can retain sulfate and limit additional water uptake (Mikhailov et al., 2009; Riemer et al., 2019). During Stage II, stronger oxidation is associated with an increase in D_{va} of about 25% and a further rise in pSNR of about 80%, again with minimal change in κ_{eff}, consistent with continued sulfate accumulation and coating growth on a compact and relatively hydrophobic matrix. In contrast, for particles with weaker organic signatures, Stage I shows more pronounced hygroscopic growth. The transition from BC-CN to BC-sec exhibits the largest κ_{eff} increase (~30%) with substantial size growth (~24%), while pSNR rises more modestly, indicating dominant inorganic uptake under ordinary conditions. In Stage II, κ_{eff} changes little, but pSNR increases markedly (~105%) and D_{va} expands to ~700 nm (~36%). This shift indicates enhanced sulfate-rich coating growth as gSNR and oxidant levels rise. For BC-free particles (BF-CN to BF-sec), pSNR changes remain small, while κ_{eff} and D_{va} increase steadily across both stages (~6% and ~22%, respectively), consistent with growth driven largely by water uptake and increased SIS loadings in the absence of BC-related pathways.

Overall, κ_{eff} and pSNR coupling strengthen under higher gSNR and stronger oxidation, but the response remains particle-type dependent. BC-containing particles can serve as efficient sulfate sinks because BC cores provide reactive surfaces for heterogeneous and photo-assisted oxidation and favor condensational coating growth. OC-containing particles may also show strong pSNR enhancement, yet these changes more often accompanied by relatively lower hygroscopicity, smaller size, and compact shell-like structures. In contrast, BC-free particles show more limited changes. As a result, different particle types may exert different atmospheric effects. More hygroscopic BC-containing particles are more likely to enhance light scattering, promote cloud droplet activation, and increase BC light absorption via the lensing effect. Under continued NO_x mitigation, which may further elevate gSNR and atmospheric oxidizing capacity, such divergence in aging pathways is likely to become more pronounced, with potential consequences for cloud albedo, precipitation formation, visibility, and boundary-layer stability (Khalizov et al., 2009; Li et al., 2020; Petäjä et al., 2016).

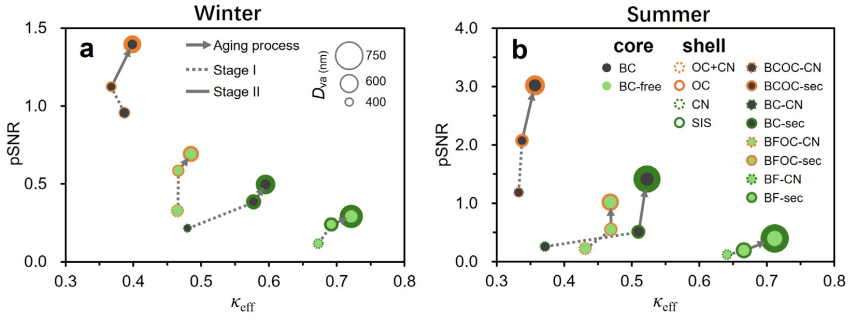

Figure 4. Co-evolution of particle-phase sulfur-to-nitrogen ratio (pSNR) and

https://doi.org/10.5194/egusphere-2026-3360
Preprint. Discussion started: 13 July 2026

hygroscopicity (κ_{eff}) for distinct particle classes during aging in winter (a) and summer (b). Particles are shown with a core-shell schematic. The inner dot indicates the core type, black carbon (BC, dark gray) or BC free (light green). The outer ring indicates the dominant coating category, organic carbon (OC, orange) or secondary inorganic species (SIS, green). Dashed rings denote fresh-like types, and solid rings denote aged-like coatings. Marker size scales with vacuum aerodynamic diameter (D_{va}). Shell thickness estimates from the D_{va} of aged-like and fresh-like particles. Arrows depict the aging pathways: Stage I (dotted lines) represents aging under normal periods (NPs) with moderate gSNR and weaker oxidation, and Stage II (solid arrows) represents additional aging under emission control periods (ECPs) with elevated gSNR and stronger oxidation.

3.4 Humidity-Driven Phase Transitions and Mixing-State Evolution Regulate Sulfur-Nitrogen Partitioning.

Ammonium sulfate (AS) and ammonium nitrate (AN) are the dominant SIS in $PM_{2.5}$(Fu et al., 2016; Lin et al., 2020). Their deliquescence relative humidity (DRH), together with the mutual deliquescence RH (MDRH) of mixed salts, sets key thresholds for particle phase transitions and the onset of aqueous processing(Liu et al., 2021; Sun et al., 2018), and these thresholds may be further influenced by organic constituents (Li et al., 2021). As RH increases, the associated rise in aerosol liquid water (ALW) lowers matrix viscosity, enhances molecular transport, and promotes morphological restructuring and internal mixing (Mikhailov et al., 2009; Shiraiwa et al., 2011). In our observations, increasing RH is accompanied by generally declining and progressively converging gSNR, pSNR, and nSNR, indicating a shift toward more balanced S-N partitioning across gas, particle, and number domains (**Figure S4a, e**). In parallel, BCOC-sec consistently exhibits the highest pSNR and nSNR, while BF-sec remains the lowest, but these contrasts weaken as RH increases, suggesting that elevated humidity reduces particle-type compositional and population-level contrasts of S-N partitioning (**Figure S4b, f**). Guided by these physicochemical thresholds and the observed SNR evolution, we interpret the RH continuum using four characteristic regimes (**Figure 5**).

Low-RH regime (RH < 55%, solid phase). Under dry conditions, particles are largely solid with negligible ALW and limited ionic mobility (Sun et al., 2018). Uptake of HNO_3 and N_2O_5 hydrolysis is suppressed, restricting particulate nitrate formation (Bertram and Thornton, 2009), while SO_2 oxidation on BC and mineral surfaces proceeds slowly (He et al., 2018; Zhao et al., 2017). High solar radiation in this regime favors particulate nitrate photolysis, generating OH radicals that can drive heterogeneous SO_2 oxidation (He et al., 2017; Ye et al., 2017). As a result, pSNR is locally elevated, particularly in BCOC-sec, where BC serves as a photochemically active substrate enhancing sulfate formation, while OC acts as a stabilizing matrix that

https://doi.org/10.5194/egusphere-2026-3360
Preprint. Discussion started: 13 July 2026

retains sulfate internally (**Section 3.2**). Weak correlations among gSNR, pSNR and nSNR (**Figure S5**) indicate kinetic limitations on gas-particle mass transfer and the particle population remains externally mixed with pronounced differences in nSNR across particle types (**Figure S4c, g**).

Moderate RH regime I (RH ≈ 55–70%, onset of NH_4NO_3 deliquescence). Crossing the DRH of AN (~61%) induces a solid to semi-solid transition, forming a reactive aqueous surface film (Seinfeld and Pandis, 2016). These films relax interfacial diffusion constraints and enhance ionic mobility, activating solid particles by rapid water uptake, which is consistent with increases in particle size and number concentration (**Figure S4d, h**). ALW on BC surfaces may dissociate to OH radicals, while O_3, H_2O_2 and NO_2 oxidation pathways further enhance sulfate formation (He and He, 2020; J. Wang et al., 2020). Because NH_3 tends to neutralize H_2SO_4 preferentially, sulfate can remain relatively favored during the early stage of humidification, even as nitrate production increases (Wang et al., 2013; Seinfeld and Pandis, 2016). Accordingly, pSNR rises, most strongly in BC-containing classes such as BC-sec and BCOC-sec (**Figure S4b, f**).

Moderate RH regime II (RH ≈ 70–85%, enhanced multiphase reactions). As RH approaches the MDRH of AS-AN mixtures (69–75%), semi-solid particles transition toward fully liquid states with substantial ALW uptake and bulk-phase processing (Sun et al., 2018). This phase transition promotes efficient internal mixing and SIS shell formation (Riemer et al., 2019), driving particle growth and increased number concentration primarily through condensational uptake between ~60–75% RH (**Figure S4d, h**). Once H_2SO_4 is largely neutralized, excess NH_3 facilitates NH_4NO_3 formation (Seinfeld and Pandis, 2016). High ALW and elevated effective Henry's law constants enhance HNO_3 uptake, while NO_2 hydrolysis and heterogeneous N_2O_5 reactions accelerate nitrate accumulation (Bertram and Thornton, 2009). These processes progressively shift S-N partitioning toward nitrogen, lowering pSNR from its peak near 70% RH. Concurrently, the differences among gSNR, pSNR, and nSNR narrow, suggesting that gas-particle S-N partitioning increasingly approaches quasi-equilibrium and cross-phase coupling strengthens (**Figure 5**). Around 80% RH, both D_{va} and particle number concentration show a sharp and transient decline, likely reflecting enhanced coagulation, temporarily reduced net condensational growth (El Haber et al., 2024), and liquid-coating-induced restructuring (e.g., capillary compaction of loose aggregates into denser particles) (Chen et al., 2016; Beeler et al., 2025).

High-RH regime (RH > 85%, liquid phase). Exceeding the DRH of AS (~80 %) (Lightstone et al., 2000) induces a predominantly aqueous particle phase (Bateman et al., 2016; Sun et al., 2018). Under these conditions, dissolution of reactive precursors is favored and kinetic barriers to gas-to-particle partitioning are strongly reduced (Seinfeld and Pandis, 2016), leading to much tighter coupling among gSNR, pSNR, and nSNR (R^2 ranged from 0.68 to 0.81, **Figure S5**). All three SNR metrics converge

https://doi.org/10.5194/egusphere-2026-3360
Preprint. Discussion started: 13 July 2026

to similarly low and relatively stable values (**Figure 5**), consistent with more efficient cross-phase exchange and multiphase processing. Particle-type SNR curves (**Figure S4b, c, f, g**) show minimal divergence, reflecting extensive internal mixing that homogenizes particle composition and convergence of external mixing states across the population. Near saturation, continued water uptake increases particle size and may enhance wet removal (e.g., fog/precipitation-related scavenging), contributing to reduced number concentrations (**Figure S4d, h**).

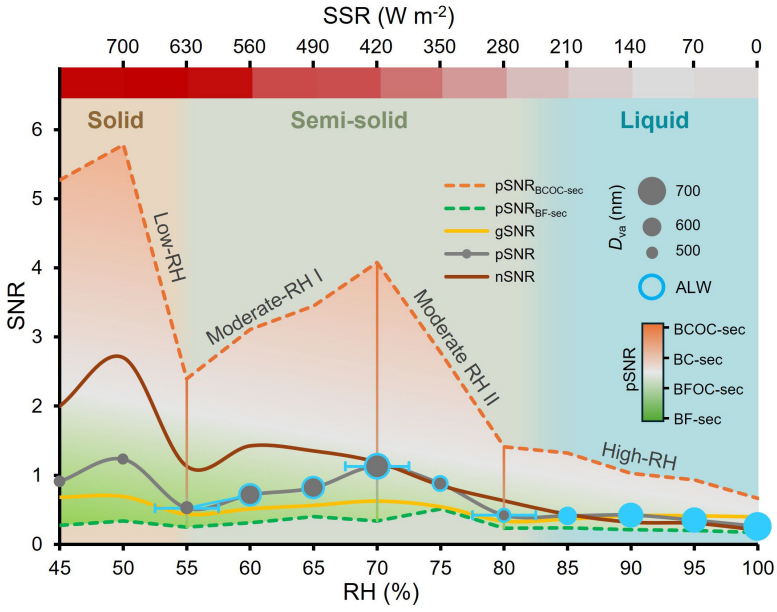

Figure 5 . Phase-state-resolved variations of sulfur-to-nitrogen ratios (SNRs) and particle physicochemical properties as a function of relative humidity (RH). Shown are RH-dependent evolutions of gas-phase (gSNR, yellow), particle-phase (pSNR, grey), and number-based (nSNR, brown), overlaid with pSNR of representative particle classes: BCOC-sec (orange dashed) and BF-sec (green dashed). Color shading beneath the curves denotes the relative magnitude of pSNR, following the sequence BCOC-sec > BC-sec > BFOC-sec > BF-sec. The RH regimes are classified as Low RH (< 55%), Moderate RH (55–70% and 70–85%), and high RH (> 85%), with the top red gradient bar indicating mean surface solar radiation (SSR). Circular markers represent average particle size (bubble size: D_{va}), phase state (grey: solid; grey with blue ring: semi-solid; blue: liquid), and aerosol liquid water (ALW, blue ring). Vertical lines mark the DRH of NH_4NO_3 (AN), the MDRH of $(NH_4)_2SO_4$-NH_4NO_3 mixtures (AN-SN), and the DRH of $(NH_4)_2SO_4$ (SN); error bars represent variability among literature reports and temperature-dependent shifts.

https://doi.org/10.5194/egusphere-2026-3360
Preprint. Discussion started: 13 July 2026

3.5 Causal Inference and Machine-Learning Interpretation of Key Drivers

Causal Network Insights. From the ten meteorological and chemical descriptors (**Table S2**), the GS algorithm selected eight key predictors: O_3, T2m, SSR, RH, WS, WD, SLP, and BLH. Applying the GES to this subset produced the DAGs in **Figure 6**. In the DAGs, arrow direction denotes causal influence, arrow color encodes the sign of association (red for positive, grey for negative), and arrow thickness scales with the absolute Pearson correlation between connected variables. The DAG analysis identifies a consistent hierarchical dependency spanning from gSNR to pSNR and further to nSNR. While these arrows indicate the most probable direction of influence under current statistical constraints, they represent the sequential propagation of chemical signals from gas-phase precursors to particle-level composition and then reshapes the population-level mixing state, consistent with the mechanistic picture developed in **Sections 3.2-3.4**, but may still be affected by unmeasured factors (e.g., NH_3 availability or heterogeneous kinetics) that are not explicitly represented in the network.

In addition, O_3 and BLH occupy intermediate positions between the SNR metrics and the meteorological cluster (RH, T2m, SSR, SLP), indicating that oxidant levels and boundary-layer dynamics may mediate the influence of radiation and stability on S-N partitioning. RH, T2m and SSR form a densely connected sub-network with predominantly negative links between RH, T2m and SSR, consistent with the anti-correlation between humidity and temperature/solar radiation. WS and WD show weaker and more diffuse connections, suggesting a secondary role through transport and dispersion. Overall, the DAG indicates that precursor ratios, oxidant levels and boundary-layer structure jointly organize the progression from gas-phase composition to particle-phase and number-based SNR metrics.

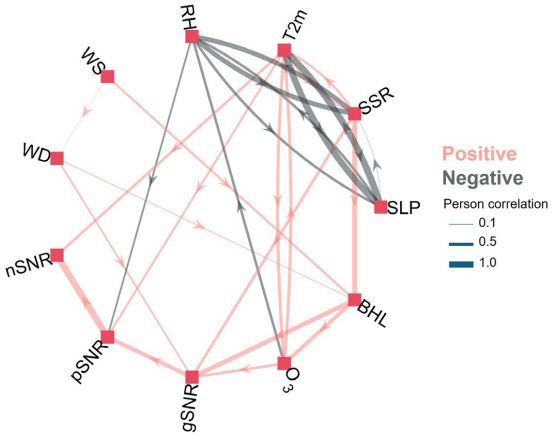

Figure 6. Causal network revealing key drivers of sulfur-to-nitrogen ratios (SNRs) across atmospheric phases. Red and gray arrows denote positive and negative

https://doi.org/10.5194/egusphere-2026-3360
Preprint. Discussion started: 13 July 2026

correlations, respectively, with line thickness scaled to correlation strength.

Model Performance Validation. To complement the causal analysis and capture nonlinear interactions, we trained particle-class-specific models using an SSA-optimized XGBoost framework. Cross-validated performance statistics (**Table S4**) show R^2 values above 0.70 with low RMSE for all three SNR metrics, indicating robust predictive skill across different particle types and limited overfitting.

SHAP-based Driver Attribution. To quantify the relative influence of candidate drivers, we examined SHAP values for each SNR metric. As shown in **Figure S6a-d**, gSNR is the dominant determinant of particle-phase S-N partitioning, with the strongest influence for BC-sec, where large SHAP magnitudes suggest tight sensitivity of BC-containing particles to gas-phase composition. In the number domain (nSNR; **Figure S6e-h**), pSNR is the leading contributor across all aged-like classes, supporting a sequential response in which gas-phase variability first modulates within-particle S-N balance (pSNR) and is subsequently expressed at the population level (nSNR), consistent with the causal pathway inferred in **Section 3.5**.

Meteorological factors exert secondary, modulatory influences on SNR metrics. RH shows a consistent negative effect, reflecting enhanced nitrate formation and dilution under humid conditions. Conversely, SSR and O_3 contribute positively (**Figure S6b, f**), indicating the promotion of photochemistry activity and SO_2 oxidation (Seinfeld and Pandis, 2016; He et al., 2014). WD and BLH generally contribute negatively, capturing the dilution and vertical mixing effects that suppress SNR metrics (**Figure S6c, g**).

4. Conclusions and implications

This work establishes a cross-domain linkage among sulfur-to-nitrogen ratios in the gas phase (gSNR), particle phase (pSNR), and single-particle populations (nSNR), revealing a stepwise propagation from precursor composition to particle chemistry and, ultimately to mixing-state evolution. Although shifts in gSNR impose a first-order constraint on S-N partitioning, the realized aerosol response remains strongly particle-type dependent. BC-containing and OC-containing particles exhibit more pronounced sulfate enrichment, whereas BC-free particles show much weaker compositional adjustment under comparable precursor perturbations. These results demonstrate that SNR coupling is governed not only by precursor ratios, but also by particle composition and particle-type-specific properties.

Relative humidity (RH) emerges as the primary environmental regulator of this multiphase coupling by modulating phase transitions, aerosol liquid water (ALW), and ionic mobility. Under dry conditions (RH<55%), limited ALW suppresses cross-phase propagation, leading to pronounced decoupling among gSNR, pSNR, and nSNR and

https://doi.org/10.5194/egusphere-2026-3360
Preprint. Discussion started: 13 July 2026

sustaining a largely externally mixed aerosol population. As RH rises into the deliquescence regime (55–85%), increasing ALW promotes internal mixing and accelerates multiphase processing. At high RH (> 85%), the system tends toward convergence, with closer alignment among gSNR, pSNR, and nSNR and reduced particle-type contrasts.

These findings have important implications for regional air-quality modeling. The humidity-dependent coupling of cross-phase SNR coupling indicates that, under low-humidity conditions, thermodynamic-equilibrium-based frameworks may misrepresent secondary inorganic species (SIS) formation when rapid equilibration and compositionally well-mixed particles are assumed. Our results therefore suggest a need for RH- and phase-state-dependent treatments of S-N partitioning and SIS formation, together with more explicit representation of particle-type and mixing-state heterogeneity under dry conditions. Under humid conditions, the tighter coupling among gas- and particle-phase SNR implies that gSNR may better represent population-mean particle SNR, suggesting improved model performance when humidity-dependent constraints are considered.

Data availability. All data supporting the findings of this study are available within the paper and its Supplementary Information. Additional data related to this paper are available on request by contacting the corresponding author Xinlei Ge (xinlei@seu.edu.cn) and Junfeng Wang (wangjunfeng@nuist.edu.cn).

Supplement. The supplement related to this article is available online at: XXX.

Author contributions. X.G., M.C., and J.W. conceptualized the study and designed the research. Y.D. and S.Z. conducted the field experiments. Y.D. and J.W. analyzed the data and prepared the original draft of the manuscript. X.G., M.C., H.L., Y.W., Y.Z., and M.W. reviewed and edited the manuscript.

Competing Interest. The authors declare no competing financial interest.

Financial support. This study was supported by the National Natural Science Foundation of China (Grant Nos. U24A20515, 22361162668, 22276099 and 42405106).

https://doi.org/10.5194/egusphere-2026-3360
Preprint. Discussion started: 13 July 2026

References

Bateman, A.P., Gong, Z., Liu, P., Sato, B., Cirino, G., Zhang, Y., Artaxo, P., Bertram, A.K., Manzi, A.O., Rizzo, L.V., Souza, R.A.F., Zaveri, R.A., Martin, S.T., 2016. Sub-micrometre particulate matter is primarily in liquid form over Amazon rainforest. Nat. Geosci. 9, 34–37. https://doi.org/10.1038/ngeo2599

Beeler, P., Corbin, J.C., Sipkens, T.A., Fierce, L., 2025. A framework for quantifying the size and fractal dimension of compacting soot particles. Environ. Sci. Technol. 59, 5994–6003. https://doi.org/10.1021/acs.est.4c11100

Bertram, T.H., Thornton, J.A., 2009. Toward a general parameterization of N_2O_5 reactivity on aqueous particles: The competing effects of particle liquid water, nitrate and chloride. Atmospheric Chem. Phys. 9, 8351–8363. https://doi.org/10.5194/acp-9-8351-2009

Bi, X., Zhang, G., Li, L., Wang, X., Li, M., Sheng, G., Fu, J., Zhou, Z., 2011. Mixing state of biomass burning particles by single particle aerosol mass spectrometer in the urban area of PRD, China. Atmos. Environ. 45, 3447–3453. https://doi.org/10.1016/j.atmosenv.2011.03.034

Chen, C., Fan, X., Shaltout, T., Qiu, C., Ma, Y., Goldman, A., Khalizov, A.F., 2016. An unexpected restructuring of combustion soot aggregates by subnanometer coatings of polycyclic aromatic hydrocarbons. Geophys. Res. Lett. 43, 11,080-11,088. https://doi.org/10.1002/2016GL070877

Cheng, Y., Zheng, G., Wei, C., Mu, Q., Zheng, B., Wang, Z., Gao, M., Zhang, Q., He, K., Carmichael, G., Pöschl, U., Su, H., 2016. Reactive nitrogen chemistry in aerosol water as a source of sulfate during haze events in China. Sci. Adv. 2, e1601530. https://doi.org/10.1126/sciadv.1601530

Chickering, D.M., 2003. Optimal structure identification with greedy search. J Mach Learn Res 3, 507–554. https://doi.org/10.1162/153244303321897717

Chu, B., Ma, Q., Liu, J., Ma, Jinzhu, Zhang, P., Chen, T., Feng, Q., Wang, C., Yang, N., Ma, H., Ma, Jingjin, Russell, A.G., He, H., 2020. Air pollutant correlations in China: Secondary air pollutant responses to NO_x and SO_2 control. Environ. Sci. Technol. Lett. 7, 695–700. https://doi.org/10.1021/acs.estlett.0c00403

Dai, Y., Wang, J., Wang, H., Cui, S., Zhang, Y., Li, H., Wu, Y., Wang, M., Aruffo, E., Ge, X., 2024. Measurement report: Characteristics of airborne black-carbon-containing particles during the 2021 summer COVID-19 lockdown in a typical Yangtze River Delta city, China. Atmospheric Chem. Phys. 24, 9733–9748. https://doi.org/10.5194/acp-24-9733-2024

Ekanayake, I.U., Meddage, D.P.P., Rathnayake, U., 2022. A novel approach to explain the black-box nature of machine learning in compressive strength predictions of concrete using shapley additive explanations (SHAP). Case Stud. Constr. Mater. 16, e01059. https://doi.org/10.1016/j.cscm.2022.e01059

El Haber, M., Gérard, V., Kleinheins, J., Ferronato, C., Nozière, B., 2024. Measuring the surface tension of atmospheric particles and relevant mixtures to better

https://doi.org/10.5194/egusphere-2026-3360
Preprint. Discussion started: 13 July 2026

understand key atmospheric processes. Chem. Rev. 124, 10924–10963. https://doi.org/10.1021/acs.chemrev.4c00173

El Haddad, I., Vienneau, D., Daellenbach, K.R., Modini, R., Slowik, J.G., Upadhyay, A., Vasilakos, P.N., Bell, D., de Hoogh, K., Prevot, A.S.H., 2024. Opinion: How will advances in aerosol science inform our understanding of the health impacts of outdoor particulate pollution? Atmospheric Chem. Phys. 24, 11981–12011. https://doi.org/10.5194/acp-24-11981-2024

Fu, X., Wang, S., Chang, X., Cai, S., Xing, J., Hao, J., 2016. Modeling analysis of secondary inorganic aerosols over China: Pollution characteristics, and meteorological and dust impacts. Sci. Rep. 6, 35992. https://doi.org/10.1038/srep35992

Geng, G., Liu, Yuxi, Liu, Yang, Liu, S., Cheng, J., Yan, L., Wu, N., Hu, H., Tong, D., Zheng, B., Yin, Z., He, K., Zhang, Q., 2024. Efficacy of China's clean air actions to tackle $PM_{2.5}$ pollution between 2013 and 2020 air actions. Nat. Geosci. 17, 987–994. https://doi.org/10.1038/s41561-024-01540-z

George, I.J., Abbatt, J.P.D., 2010. Heterogeneous oxidation of atmospheric aerosol particles by gas-phase radicals. Nat. Chem. 2, 713–722. https://doi.org/10.1038/nchem.806

He, G., He, H., 2020. Water promotes the oxidation of SO_2 by O_2 over carbonaceous aerosols. Environ. Sci. Technol. 54, 7070–7077. https://doi.org/10.1021/acs.est.0c00021

He, G., Ma, J., He, H., 2018. Role of carbonaceous aerosols in catalyzing sulfate formation. ACS Catal. 8, 3825–3832. https://doi.org/10.1021/acscatal.7b04195

He, H., Wang, Y., Ma, Q., Ma, J., Chu, B., Ji, D., Tang, G., Liu, C., Zhang, H., Hao, J., 2014. Mineral dust and NO_x promote the conversion of SO_2 to sulfate in heavy pollution days. Sci. Rep. 4, 4172. https://doi.org/10.1038/srep04172

He, X., Pang, S., Ma, J., Zhang, Y., 2017. Influence of relative humidity on heterogeneous reactions of O_3 and O_3/SO_2 with soot particles: Potential for environmental and health effects. Atmos. Environ. 165, 198–206. https://doi.org/10.1016/j.atmosenv.2017.06.049

Healy, R.M., Sciare, J., Poulain, L., Crippa, M., Wiedensohler, A., Prévôt, A.S.H., Baltensperger, U., Sarda-Estève, R., McGuire, M.L., Jeong, C.-H., McGillicuddy, E., O'Connor, I.P., Sodeau, J.R., Evans, G.J., Wenger, J.C., 2013. Quantitative determination of carbonaceous particle mixing state in Paris using single-particle mass spectrometer and aerosol mass spectrometer measurements. Atmospheric Chem. Phys. 13, 9479–9496. https://doi.org/10.5194/acp-13-9479-2013

Huang, R.-J., Zhang, Y., Bozzetti, C., Ho, K.-F., Cao, J.-J., Han, Y., Daellenbach, K.R., Slowik, J.G., Platt, S.M., Canonaco, F., Zotter, P., Wolf, R., Pieber, S.M., Bruns, E.A., Crippa, M., Ciarelli, G., Piazzalunga, A., Schwikowski, M., Abbaszade, G., Schnelle-Kreis, J., Zimmermann, R., An, Z., Szidat, S., Baltensperger, U., Haddad, I.E., Prévôt, A.S.H., 2014. High secondary aerosol contribution to particulate pollution during haze events in China. Nature 514, 218–222.

https://doi.org/10.5194/egusphere-2026-3360
Preprint. Discussion started: 13 July 2026

https://doi.org/10.1038/nature13774

Huang, X., Ding, A., Gao, J., Zheng, B., Zhou, D., Qi, X., Tang, R., Wang, J., Ren, C., Nie, W., Chi, X., Xu, Z., Chen, L., Li, Y., Che, F., Pang, N., Wang, H., Tong, D., Qin, W., Cheng, W., Liu, W., Fu, Q., Liu, B., Chai, F., Davis, S.J., Zhang, Q., He, K., 2021. Enhanced secondary pollution offset reduction of primary emissions during COVID-19 lockdown in China. Natl. Sci. Rev. 8, nwaa137. https://doi.org/10.1093/nsr/nwaa137

Huang, X., Liu, Z., Ge, Y., Li, Q., Wang, Xiaofei, Fu, H., Zhu, J., Zhou, B., Wang, L., George, C., Wang, Y., Wang, Xinfeng, Su, J., Xue, L., Yu, S., Mellouki, A., Chen, J., 2023. Aerosol high water contents favor sulfate and secondary organic aerosol formation from fossil fuel combustion emissions. Npj Clim. Atmospheric Sci. 6, 173. https://doi.org/10.1038/s41612-023-00504-1

Khalizov, A.F., Xue, H., Wang, L., Zheng, J., Zhang, R., 2009. Enhanced light absorption and scattering by carbon soot aerosol internally mixed with sulfuric acid. J. Phys. Chem. A 113, 1066–1074. https://doi.org/10.1021/jp807531n

Koller, D., 2009. Probabilistic graphical models: Principles and techniques - adaptive computation and machine learning. The MIT Press.

Le, T., Wang, Y., Liu, L., Yang, J., Yung, Y.L., Li, G., Seinfeld, J.H., 2020. Unexpected air pollution with marked emission reductions during the COVID-19 outbreak in China. Science 369, 702–706. https://doi.org/10.1126/science.abb7431

Li, Jiawei, Han, Z., Wu, Y., Xiong, Z., Xia, X., Li, Jie, Liang, L., Zhang, R., 2020. Aerosol radiative effects and feedbacks on boundary layer meteorology and $PM_{2.5}$ chemical components during winter haze events over the Beijing-Tianjin-Hebei Region. Atmospheric Chem. Phys. 20, 8659–8690. https://doi.org/10.5194/acp-20-8659-2020

Li, K., Jacob, D.J., Liao, H., Shen, L., Zhang, Q., Bates, K.H., 2019. Anthropogenic drivers of 2013–2017 trends in summer surface ozone in China. Proc. Natl. Acad. Sci. 116, 422–427. https://doi.org/10.1073/pnas.1812168116

Li, W., Teng, X., Chen, X., Liu, L., Xu, L., Zhang, J., Wang, Y., Zhang, Y., Shi, Z., 2021. Organic coating reduces hygroscopic growth of phase-separated aerosol particles. Environ. Sci. Technol. 55, 16339–16346. https://doi.org/10.1021/acs.est.1c05901

Liang, X., Zhang, S., Wu, Y., Xing, J., He, X., Zhang, K.M., Wang, S., Hao, J., 2019. Air quality and health benefits from fleet electrification in China. Nat. Sustain. 2, 962–971. https://doi.org/10.1038/s41893-019-0398-8

Liang, Z., Zhang, R., Gen, M., Chu, Y., Chan, C.K., 2021. Nitrate photolysis in mixed sucrose–nitrate–sulfate particles at different relative humidities. J. Phys. Chem. A 125, 3739–3747. https://doi.org/10.1021/acs.jpca.1c00669

Lightstone, J.M., Onasch, T.B., Imre, D., Oatis, S., 2000. Deliquescence, efflorescence, and water activity in ammonium nitrate and mixed ammonium nitrate/succinic acid microparticles. J. Phys. Chem. A 104, 9337–9346. https://doi.org/10.1021/jp002137h

Lin, C., Huang, R.-J., Zhong, H., Duan, J., Wang, Z., Huang, W., Xu, W., 2023.

https://doi.org/10.5194/egusphere-2026-3360
Preprint. Discussion started: 13 July 2026

Elucidating ozone and $PM_{2.5}$ pollution in the Fenwei plain reveals the co-benefits of controlling precursor gas emissions in winter haze. Atmospheric Chem. Phys. 23, 3595–3607. https://doi.org/10.5194/acp-23-3595-2023

Lin, Y.-C., Zhang, Y.-L., Fan, M.-Y., Bao, M., 2020. Heterogeneous formation of particulate nitrate under ammonium-rich regimes during the high-$PM_{2.5}$ events in Nanjing, China. Atmospheric Chem. Phys. 20, 3999–4011. https://doi.org/10.5194/acp-20-3999-2020

Ling, Z., Yu, K., Zhang, Y., Liu, L., Li, J., 2022. Causal learner: A toolbox for causal structure and markov blanket learning. Pattern Recognit. Lett. 163, 92–95. https://doi.org/10.1016/j.patrec.2022.09.021

Liu, P., Li, Y.J., Wang, Y., Bateman, A.P., Zhang, Y., Gong, Z., Bertram, A.K., Martin, S.T., 2018. Highly viscous states affect the browning of atmospheric organic particulate matter. ACS Cent. Sci. 4, 207–215. https://doi.org/10.1021/acscentsci.7b00452

Liu, P., Ye, C., Xue, C., Zhang, C., Mu, Y., Sun, X., 2020. Formation mechanisms of atmospheric nitrate and sulfate during the winter haze pollution periods in Beijing: Gas-phase, heterogeneous and aqueous-phase chemistry. Atmospheric Chem. Phys. 20, 4153–4165. https://doi.org/10.5194/acp-20-4153-2020

Liu, X., Ran, L., Lin, W., Xu, X., Ma, Z., Dong, F., He, D., Zhou, L., Shi, Q., Wang, Y., 2022. Measurement report: Variations in surface SO_2 and NO_x mixing ratios from 2004 to 2016 at a background site in the North China Plain. Atmospheric Chem. Phys. 22, 7071–7085. https://doi.org/10.5194/acp-22-7071-2022

Liu, Y., Feng, Z., Zheng, F., Bao, X., Liu, P., Ge, Y., Zhao, Y., Jiang, T., Liao, Y., Zhang, Y., Fan, X., Yan, C., Chu, B., Wang, Y., Du, W., Cai, J., Bianchi, F., Petäjä, T., Mu, Y., He, H., Kulmala, M., 2021. Ammonium nitrate promotes sulfate formation through uptake kinetic regime. Atmospheric Chem. Phys. 21, 13269–13286. https://doi.org/10.5194/acp-21-13269-2021

Lu, X., Zhang, S., Xing, J., Wang, Y., Chen, W., Ding, D., Wu, Y., Wang, S., Duan, L., Hao, J., 2020. Progress of air pollution control in China and its challenges and opportunities in the ecological civilization era. Engineering 6, 1423–1431. https://doi.org/10.1016/j.eng.2020.03.014

Margaritis, D., 1999. Bayesian network induction via local neighborhoods, in: Advances in Neural Information Processing Systems. MIT Press, pp. 505–511.

Mikhailov, E., Vlasenko, S., Martin, S.T., Koop, T., Pöschl, U., 2009. Amorphous and crystalline aerosol particles interacting with water vapor: Conceptual framework and experimental evidence for restructuring, phase transitions and kinetic limitations. Atmospheric Chem. Phys. 9, 9491–9522. https://doi.org/10.5194/acp-9-9491-2009

Nozière, B., Ekström, S., Alsberg, T., Holmström, S., 2010. Radical-initiated formation of organosulfates and surfactants in atmospheric aerosols. Geophys. Res. Lett. 37, 2009GL041683. https://doi.org/10.1029/2009GL041683

Petäjä, T., Järvi, L., Kerminen, V.-M., Ding, A.J., Sun, J.N., Nie, W., Kujansuu, J.,

https://doi.org/10.5194/egusphere-2026-3360
Preprint. Discussion started: 13 July 2026

Virkkula, A., Yang, X., Fu, C.B., Zilitinkevich, S., Kulmala, M., 2016. Enhanced air pollution via aerosol-boundary layer feedback in China. Sci. Rep. 6, 18998. https://doi.org/10.1038/srep18998

Petters, M.D., Kreidenweis, S.M., 2007. A single parameter representation of hygroscopic growth and cloud condensation nucleus activity. Atmospheric Chem. Phys. 7, 1961–1971. https://doi.org/10.5194/acp-7-1961-2007

Rickards, A.M.J., Song, Y.-C., Miles, R.E.H., Preston, T.C., Reid, J.P., 2015. Variabilities and uncertainties in characterising water transport kinetics in glassy and ultraviscous aerosol. Phys. Chem. Chem. Phys. 17, 10059–10073. https://doi.org/10.1039/C4CP05383D

Riemer, N., Ault, A.P., West, M., Craig, R.L., Curtis, J.H., 2019. Aerosol mixing state: Measurements, modeling, and impacts. Rev. Geophys. 57, 187–249. https://doi.org/10.1029/2018RG000615

Riva, M., Da Silva Barbosa, T., Lin, Y.-H., Stone, E.A., Gold, A., Surratt, J.D., 2016. Chemical characterization of organosulfates in secondary organic aerosol derived from the photooxidation of alkanes. Atmospheric Chem. Phys. 16, 11001–11018. https://doi.org/10.5194/acp-16-11001-2016

Schmedding, R., Rasool, Q.Z., Zhang, Y., Pye, H.O.T., Zhang, H., Chen, Y., Surratt, J.D., Lopez-Hilfiker, F.D., Thornton, J.A., Goldstein, A.H., Vizuete, W., 2020. Predicting secondary organic aerosol phase state and viscosity and its effect on multiphase chemistry in a regional-scale air quality model. Atmospheric Chem. Phys. 20, 8201–8225. https://doi.org/10.5194/acp-20-8201-2020

Seinfeld, J.H., Pandis, S.N., 2016. Atmospheric chemistry and physics from air pollution to climate change, Third edition. ed. John Wiley & Sons, Hoboken, New Jersey.

Sharma, N., Agarwal, A.K., Eastwood, P., Gupta, T., Singh, A.P. (Eds.), 2018. Air pollution and control, Energy, Environment, and Sustainability. Springer Singapore, Singapore. https://doi.org/10.1007/978-981-10-7185-0

Sheldon, C.S., Choczynski, J.M., Morton, K., Diaz, T.P., Davis, R.D., Davies, J.F., 2023. Exploring the hygroscopicity, water diffusivity, and viscosity of organic-inorganic aerosols – a case study on internally-mixed citric acid and ammonium sulfate particles. Environ. Sci. Atmospheres 3, 24–34. https://doi.org/10.1039/D2EA00116K

Shiraiwa, M., Ammann, M., Koop, T., Pöschl, U., 2011. Gas uptake and chemical aging of semisolid organic aerosol particles. Proc. Natl. Acad. Sci. 108, 11003–11008. https://doi.org/10.1073/pnas.1103045108

Shiraiwa, M., Li, Y., Tsimpidi, A.P., Karydis, V.A., Berkemeier, T., Pandis, S.N., Lelieveld, J., Koop, T., Pöschl, U., 2017. Global distribution of particle phase state in atmospheric secondary organic aerosols. Nat. Commun. 8, 15002. https://doi.org/10.1038/ncomms15002

Snider, G., Weagle, C.L., Murdymootoo, K.K., Ring, A., Ritchie, Y., Stone, E., Walsh, A., Akoshile, C., Anh, N.X., Balasubramanian, R., Brook, J., Qonitan, F.D., Dong,

https://doi.org/10.5194/egusphere-2026-3360
Preprint. Discussion started: 13 July 2026

J., Griffith, D., He, K., Holben, B.N., Kahn, R., Lagrosas, N., Lestari, P., Ma, Z., Misra, A., Norford, L.K., Quel, E.J., Salam, A., Schichtel, B., Segev, L., Tripathi, S., Wang, C., Yu, C., Zhang, Q., Zhang, Y., Brauer, M., Cohen, A., Gibson, M.D., Liu, Y., Martins, J.V., Rudich, Y., Martin, R.V., 2016. Variation in global chemical composition of $PM_{2.5}$: Emerging results from SPARTAN. Atmospheric Chem. Phys. 16, 9629–9653. https://doi.org/10.5194/acp-16-9629-2016

Sosa Echeverría, R., Alarcón Jiménez, A.L., Torres Barrera, M. del C., Sánchez Alvarez, P., Granados Hernandez, E., Vega, E., Jaimes Palomera, M., Retama, A., Gay, D.A., 2023. Nitrogen and sulfur compounds in ambient air and in wet atmospheric deposition at Mexico city metropolitan area. Atmos. Environ. 292, 119411. https://doi.org/10.1016/j.atmosenv.2022.119411

Sun, J., Liu, L., Xu, L., Wang, Y., Wu, Z., Hu, M., Shi, Z., Li, Y., Zhang, X., Chen, J., Li, W., 2018. Key role of nitrate in phase transitions of urban particles: Implications of important reactive surfaces for secondary aerosol formation. J. Geophys. Res. Atmospheres 123, 1234–1243. https://doi.org/10.1002/2017JD027264

Sun, J., Zhi, G., Hitzenberger, R., Chen, Y., Tian, C., Zhang, Yayun, Feng, Y., Cheng, M., Zhang, Yuzhe, Cai, J., Chen, F., Qiu, Y., Jiang, Z., Li, J., Zhang, G., Mo, Y., 2017. Emission factors and light absorption properties of brown carbon from household coal combustion in China. Atmospheric Chem. Phys. 17, 4769–4780. https://doi.org/10.5194/acp-17-4769-2017

Sun, Y., Wang, Z., Wild, O., Xu, W., Chen, C., Fu, P., Du, W., Zhou, L., Zhang, Q., Han, T., Wang, Q., Pan, X., Zheng, H., Li, J., Guo, X., Liu, J., Worsnop, D.R., 2016. "APEC blue": Secondary aerosol reductions from emission controls in Beijing. Sci. Rep. 6, 20668. https://doi.org/10.1038/srep20668

Vaden, T.D., Imre, D., Beránek, J., Shrivastava, M., Zelenyuk, A., 2011. Evaporation kinetics and phase of laboratory and ambient secondary organic aerosol. Proc. Natl. Acad. Sci. 108, 2190–2195. https://doi.org/10.1073/pnas.1013391108

Wang, H., Huang, C., Tao, W., Gao, Y., Wang, S., Jing, S., Wang, W., Yan, R., Wang, Q., An, J., Tian, J., Hu, Q., Lou, S., Pöschl, U., Cheng, Y., Su, H., 2022. Seasonality and reduced nitric oxide titration dominated ozone increase during COVID-19 lockdown in Eastern China. Npj Clim. Atmospheric Sci. 5, 1–7. https://doi.org/10.1038/s41612-022-00249-3

Wang, J., Li, J., Ye, J., Zhao, J., Wu, Y., Hu, J., Liu, D., Nie, D., Shen, F., Huang, X., Huang, D.D., Ji, D., Sun, X., Xu, W., Guo, J., Song, S., Qin, Y., Liu, P., Turner, J.R., Lee, H.C., Hwang, S., Liao, H., Martin, S.T., Zhang, Q., Chen, M., Sun, Y., Ge, X., Jacob, D.J., 2020. Fast sulfate formation from oxidation of SO_2 by NO_2 and HONO observed in Beijing haze. Nat. Commun. 11, 2844. https://doi.org/10.1038/s41467-020-16683-x

Wang, J., Ye, J., Zhang, Q., Zhao, J., Wu, Y., Li, J., Liu, D., Li, W., Zhang, Y., Wu, C., Xie, C., Qin, Y., Lei, Y., Huang, X., Guo, J., Liu, P., Fu, P., Li, Y., Lee, H.C., Choi, H., Zhang, J., Liao, H., Chen, M., Sun, Y., Ge, X., Martin, S.T., Jacob, D.J., 2021.

https://doi.org/10.5194/egusphere-2026-3360
Preprint. Discussion started: 13 July 2026

Aqueous production of secondary organic aerosol from fossil-fuel emissions in winter Beijing haze. Proc. Natl. Acad. Sci. 118, e2022179118. https://doi.org/10.1073/pnas.2022179118

Wang, X., Gemayel, R., Hayeck, N., Perrier, S., Charbonnel, N., Xu, C., Chen, H., Zhu, C., Zhang, L., Wang, L., Nizkorodov, S.A., Wang, Xinming, Wang, Z., Wang, T., Mellouki, A., Riva, M., Chen, J., George, C., 2020. Atmospheric photosensitization: A new pathway for sulfate formation. Environ. Sci. Technol. 54, 3114–3120. https://doi.org/10.1021/acs.est.9b06347

Wang, Y., Zhang, Q.Q., He, K., Zhang, Q., Chai, L., 2013. Sulfate-nitrate-ammonium aerosols over China: Response to 2000–2015 emission changes of sulfur dioxide, nitrogen oxides, and ammonia. Atmospheric Chem. Phys. 13, 2635–2652. https://doi.org/10.5194/acp-13-2635-2013

Wang, Y., Zhao, Y., Wang, Yuchen, Yu, J.-Z., Shao, J., Liu, P., Zhu, W., Cheng, Z., Li, Z., Yan, N., Xiao, H., 2021. Organosulfates in atmospheric aerosols in Shanghai, China: Seasonal and interannual variability, origin, and formation mechanisms. Atmospheric Chem. Phys. 21, 2959–2980. https://doi.org/10.5194/acp-21-2959-2021

Wen, L., Xue, L., Wang, X., Xu, C., Chen, T., Yang, L., Wang, T., Zhang, Q., Wang, W., 2018. Summertime fine particulate nitrate pollution in the North China plain: Increasing trends, formation mechanisms and implications for control policy. Atmospheric Chem. Phys. 18, 11261–11275. https://doi.org/10.5194/acp-18-11261-2018

Xie, C., He, Y., Lei, L., Zhou, W., Liu, J., Wang, Q., Xu, W., Qiu, Y., Zhao, J., Sun, J., Li, L., Li, M., Zhou, Z., Fu, P., Wang, Z., Sun, Y., 2020. Contrasting mixing state of black carbon-containing particles in summer and winter in Beijing. Environ. Pollut. 263, 114455. https://doi.org/10.1016/j.envpol.2020.114455

Xu, W., Sun, Y., Wang, Q., Zhao, J., Wang, J., Ge, X., Xie, C., Zhou, W., Du, W., Li, J., Fu, P., Wang, Z., Worsnop, D.R., Coe, H., 2019. Changes in aerosol chemistry from 2014 to 2016 in winter in Beijing: Insights from high-resolution aerosol mass spectrometry. J. Geophys. Res. Atmospheres 124, 1132–1147. https://doi.org/10.1029/2018JD029245

Yang, J., Chen, Y., Chang, L., Lü, Y., 2025. Research on data resource pricing method based on SSA-XGBoost model. J. Syst. Sci. Inf. 13, 116–136. https://doi.org/10.21078/JSSI-2024-0074

Ye, C., Zhang, N., Gao, H., Zhou, X., 2017. Photolysis of particulate nitrate as a source of HONO and NO_x. Environ. Sci. Technol. 51, 6849–6856. https://doi.org/10.1021/acs.est.7b00387

Zhang, G., Fu, Y., Peng, X., Sun, W., Shi, Z., Song, W., Hu, W., Chen, D., Lian, X., Li, L., Tang, M., Wang, X., Bi, X., 2021. Black carbon involved photochemistry enhances the formation of sulfate in the ambient atmosphere: Evidence from in situ individual particle investigation. J. Geophys. Res. Atmospheres 126, e2021JD035226. https://doi.org/10.1029/2021JD035226

https://doi.org/10.5194/egusphere-2026-3360
Preprint. Discussion started: 13 July 2026

Zhang, G., Lian, X., Fu, Y., Lin, Q., Li, L., Song, W., Wang, Z., Tang, M., Chen, D., Bi, X., Wang, X., Sheng, G., 2020. High secondary formation of nitrogen-containing organics (NOCs) and its possible link to oxidized organics and ammonium. Atmospheric Chem. Phys. 20, 1469–1481. https://doi.org/10.5194/acp-20-1469-2020

Zhang, P., Chen, T., Ma, Q., Chu, B., Wang, Y., Mu, Y., Yu, Y., He, H., 2022. Diesel soot photooxidation enhances the heterogeneous formation of H_2SO_4. Nat. Commun. 13, 5364. https://doi.org/10.1038/s41467-022-33120-3

Zhang, Y., Vu, T.V., Sun, J., He, J., Shen, X., Lin, W., Zhang, X., Zhong, J., Gao, W., Wang, Y., Fu, T.M., Ma, Y., Li, W., Shi, Z., 2020. Significant changes in chemistry of fine particles in wintertime Beijing from 2007 to 2017: Impact of clean air actions. Environ. Sci. Technol. 54, 1344–1352. https://doi.org/10.1021/acs.est.9b04678

Zhang, Y., Zhao, Y., Gao, M., Bo, X., Nielsen, C.P., 2021. Air quality and health benefits from ultra-low emission control policy indicated by continuous emission monitoring: A case study in the Yangtze River Delta Region, China. Atmospheric Chem. Phys. 21, 6411–6430. https://doi.org/10.5194/acp-21-6411-2021

Zhao, Y., Liu, Y., Ma, J., Ma, Q., He, H., 2017. Heterogeneous reaction of SO_2 with soot: The roles of relative humidity and surface composition of soot in surface sulfate formation. Atmos. Environ. 152, 465–476. https://doi.org/10.1016/j.atmosenv.2017.01.005

Zhu, J., Shang, J., Chen, Y., Kuang, Y., Zhu, T., 2020. Reactive oxygen species-related inside-to-outside oxidation of soot particles triggered by visible-light irradiation: Physicochemical property changes and oxidative potential enhancement. Environ. Sci. Technol. 54, 8558–8567. https://doi.org/10.1021/acs.est.0c01150